Editors' Suggestion

Uniaxial ferromagnetism in the kagome metal TbV_6Sn_6

Elliott Rosenberg,[1] Jonathan M. DeStefano,[1] Yucheng Guo,[2] Ji Seop Oh,[2,3] Makoto Hashimoto,[4] Donghui Lu,[4] Robert J. Birgeneau,[3] Yongbin Lee,[5] Liqin Ke,[5] Ming Yi,[2] and Jiun-Haw Chu[1]

[1]*Department of Physics, University of Washington, Seattle, Washington 98195, USA*
[2]*Department of Physics and Astronomy, Rice University, Houston, Texas 77005, USA*
[3]*Department of Physics, University of California, Berkeley, California 94720, USA*
[4]*Stanford Synchrotron Radiation Lightsource, SLAC National Accelerator Laboratory, Menlo Park, California 94025, USA*
[5]*Ames Laboratory, U.S. Department of Energy, Ames, Iowa 50011, USA*

(Received 29 May 2022; revised 9 August 2022; accepted 6 September 2022; published 22 September 2022)

The synthesis and characterization of the vanadium-based kagome metal TbV_6Sn_6 is presented. X-ray measurements confirm that this material forms with the same crystal structure type as the recently investigated kagome metals GdV_6Sn_6 and YV_6Sn_6, with space group symmetry $P6/mmm$. A signature of a phase transition at 4.1 K is observed in heat capacity, resistivity, and magnetic susceptibility measurements, and both resistivity and magnetization measurements exhibit hysteresis in magnetic field. Furthermore, a strikingly large anisotropy in the magnetic susceptibility was observed, with the c-axis susceptibility roughly 75 times the ab plane susceptibility at 5 K. This is highly suggestive of uniaxial ferromagnetism, and the large size of $9.4\mu_b$/f.u. indicates the Tb^{3+} $4f$ electronic moments cooperatively align perpendicular to the V kagome lattice plane. The entropy at the phase transition is nearly R ln(2), indicating that the crystalline electric field ground state of the Tb^{3+} ion is a doublet, and therefore the sublattice of $4f$ electrons in this material can be shown to map at low temperatures to the Ising model in a D_{6h} symmetry environment. Hall measurements at temperatures from 300 to 1.7 K can be described by two-band carrier transport at temperatures below around 150 K, with a large increase in both hole and electron mobilities, similar to YV_6Sn_6, and an anomalous Hall effect is seen below the ordering temperature. Angle-resolved photoemission measurements above the magnetic ordering temperature reveal typical kagome dispersions. Our study presents TbV_6Sn_6 as an interesting system where Ising ferromagnetism coexists with nontrivial electronic states emerging from a kagome lattice.

DOI: 10.1103/PhysRevB.106.115139

I. INTRODUCTION

Recently, metals containing kagome lattices have gained attention due to the appearance of Dirac points, van Hove singularities, and geometrically driven flat bands in their resulting band structures [1–8]. Many of these materials are candidates to exhibit correlation-driven topological magnetism. In particular, members of the RT_6X_6 subset of these materials form with kagome layers comprised solely of transition-metal sites (T), potentially enabling the study of idealized pristine kagome lattices. These materials host an interplay between the nontrivial topological band structure effects that arise from the kagome sublattice, and magnetism originating from potentially large $4f$ moments in the rare-earth (R) site and $3d$ moments in the transition-metal sites. This includes the T = Mn set of recently investigated materials, in which $TbMn_6Sn_6$ exhibited robust Chern topological magnetism [9], and the other rare-earth substitutions have shown similar effects, including a large anomalous Hall effect (AHE) [10,11]. A similar set of materials, but with nonmagnetic V substituted for Mn in the intermetallic T site, might very well promise similar physics with a cleaner separation of magnetic and electronic subsystems. Recently, GdV_6Sn_6 and YV_6Sn_6 have been experimentally investigated [12,13], with the Gd member undergoing ferromagnetic order at 5 K, and a calculated band structure suggestive of hosting nontrivial topological phases. In addition, ScV_6Sn_6 was found to undergo a charge-density-wave phase transition reminiscent of the CsV_3Sb_5 system [14]. Angle-resolved photoemission spectroscopy (ARPES) experiments on GdV_6Sn_6 and HoV_6Sn_6 show the characteristic Dirac cone, saddle point, and flat bands of a kagome lattice from the purely vanadium kagome layer [15]. Furthermore, the GdV_6Sn_6 topologically nontrivial Dirac surface states have been manipulated such that the Dirac points of these states cross the Fermi energy [16]. These results imply that the RV_6Sn_6 family presents an ideal platform to study kagome physics.

It has been recently noted that the kagome materials can be manipulated via different rare-earth substitutions to provide different lattice spacings as well as tune $4f$ interactions with the transition-metal kagome network. Notably, anomalous Hall contributions to the Hall resistivity appear in some but not all of these materials [11,17], indicating the sensitive nature of the interplay between $4f$ magnetism and the geometrically driven topological band structure effects from the kagome lattice. In particular, the out-of-plane uniaxial ferrimagnetism in $TbMn_6Sn_6$ [18] is critical for realizing the spinless Haldane model that generates the Chern gapped Dirac

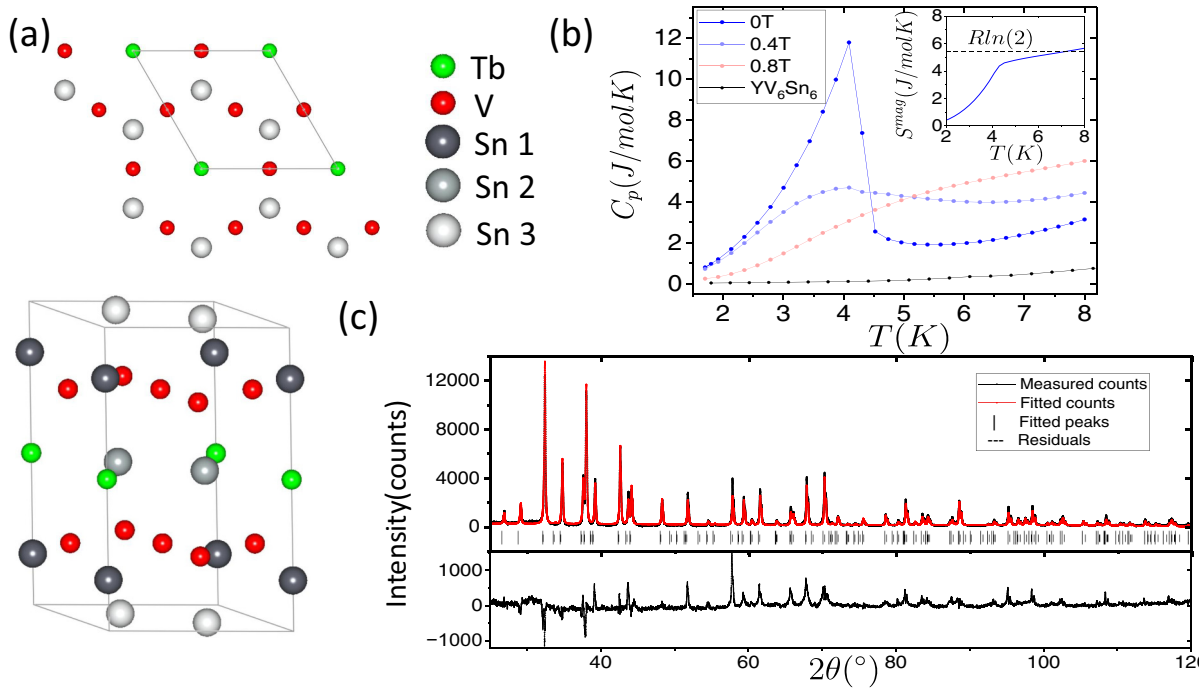

FIG. 1. (a) The crystal structure of TbV_6Sn_6, which is of the $MgFe_6Ge_6$ crystal structure type with $P6/mmm$ symmetry, with a view along the z-axis at the top (Tb sites are shown at the corners of the unit cell as opposed to Sn1 sites for clarity). (b) The heat capacity measurements of TbV_6Sn_6 at various magnetic fields applied along the c-axis from 0 to 0.8 T. For the heat capacity at 0 T, a sharp mean-field-like step is observed at 4.1 K. The inset depicts the magnetic entropy (integrated from C_p/T, which was interpolated assuming it is a smooth monotonic function of temperature with value 0 at 0 K). Note that this integration was done after removing the heat capacity from YV_6Sn_6, a nonmagnetic analog of TbV_6Sn_6. It approaches near the value R ln(2) at the phase transition. (c) The top panel shows the x-ray diffraction spectrum obtained by powdered samples, with the refined structure fit shown in red ($R = 0.203$) and alongside ticks that show the accounted peaks. The bottom panel shows the residuals of this fit.

fermions. Such a magnetic state has not been observed in the RV_6Sn_6 materials discovered so far. This motivates looking at the series of vanadium-based kagome lattices, and we pursue this by synthesizing and characterizing TbV_6Sn_6, which exhibits out-of-plane uniaxial ferromagnetism at 4.1 K.

II. METHODS

Single crystals of TbV_6Sn_6 were synthesized via the self-flux method, with Sn used as the excess flux. Mixtures of Tb (99.999%) pieces, V pieces (99.7%), and Sn shot (99.999%) were loaded into a fritted alumina crucible (CCS) [19] with atomic ratios 4.5:27:95.5, then vacuum-sealed in quartz tubes. These were heated up to 1200 °C, held there for 12 h, then slowly cooled to 600 °C in 200 h where the growths were decanted in a centrifuge to separate the excess flux from the crystals.

Powder x-ray diffraction measurements were performed on crushed single crystals using the Rigaku MiniFlex 600 system, with a Cu source and Hy-Pix 400MF 2D-detector. The lattice parameters and crystal structure type were determined via structural refinements using the MAUD software package [20].

Heat capacity measurements were carried out using the Heat Capacity option of the Quantum Design Dynacool Physical Property Measurement System (PPMS). A 1.6 mg platelike single crystal was thermally anchored to the platform using N-grease.

Magnetization measurements were performed via the Vibrating Sample Magnetometer (VSM) option of the PPMS. For field in-plane measurements, the sample was glued to a quartz paddle using two-part epoxy (to prevent the sample from being torn off at high magnetic fields due to the torque from magnetic anisotropy). For field out-of-plane measurements, samples were secured using G.E. Varnish on quartz pieces, which were held by a brass sample holder. Multiple measurements on different samples were done to confirm the magnetic anisotropy of TbV_6Sn_6, although the data in Fig. 2 are from the same sample for both in-plane and out-of-plane measurements to minimize relative errors from weighing.

Transport measurements were performed on samples that were polished and cut by a wire saw to be bar-shaped with dimensions roughly 1 mm × 0.4 mm × 0.05 mm. HCl acid (6 M) was used to remove excess Sn flux off the surface of the crystals. Silver paste and gold wires were used to make four- and five-point (Hall pattern) measurements. These measurements were performed in a Dynacool PPMS at temperatures from 300 to 1.7 K and in magnetic fields up to 14 T.

Angle-resolved photoemission spectroscopy (ARPES) measurements were performed using a DA30L analyzer at Beamline 5-2 of the Stanford Synchrotron Radiation Lightsource (SSRL) with an energy resolution of 15 meV and an angular resolution of 0.1°. The samples were cleaved *in situ* and measured with a base pressure below 3×10^{-11} Torr at 15 K.

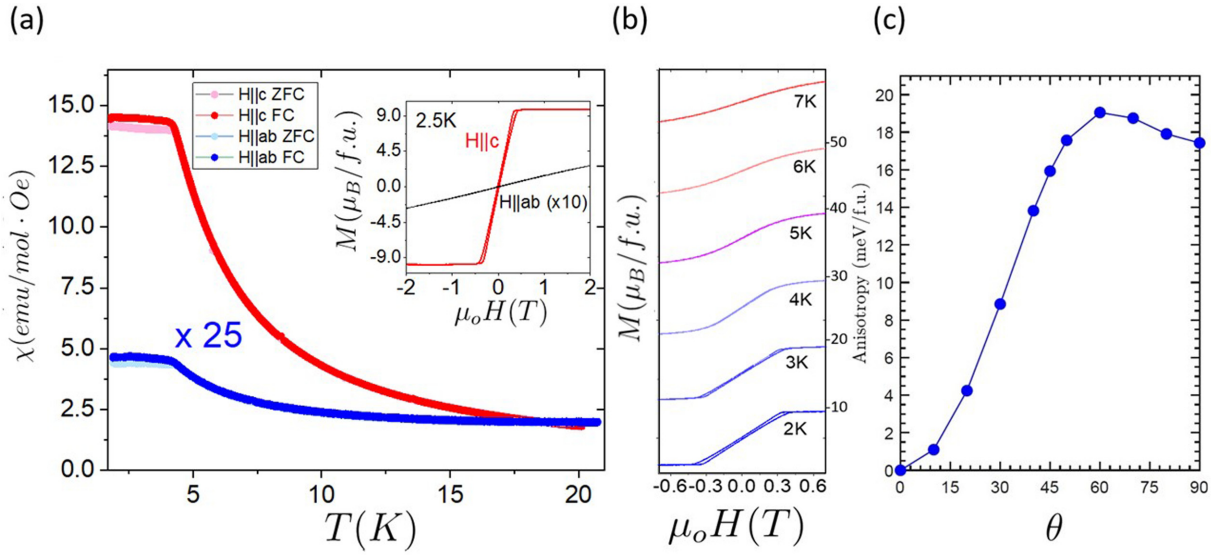

FIG. 2. (a) Magnetic susceptibility measured at 500 Oe, with the red curves indicating that the magnetic field is along the *c*-axis and the blue curves (multiplied by 25) with the field along the *ab*-plane. ZFC and FC measurements were performed, and hysteretic behavior indicative of domains is present for both orientations. The inset contains moment vs field data at 2.5 K with the field along the *c*-axis in red and the field along the *ab*-plane in black (multiplied by 10). (b) The magnetic moment in μ_B/f.u. vs magnetic field applied along the *c*-axis at temperatures from 2 to 7 K, offset by $10\mu_B$/f.u. for clarity. Hysteresis is observed at temperatures below the phase transition at 4.1 K, but not above. (c) Calculated magnetic anisotropy energy as a function of angle θ from the *c*-axis.

To compare with band structures measured in ARPES, we calculated and projected bands onto the surface Brillouin zone (BZ) by integrating the **k**-dependent spectral function $\delta[\omega - E_i(\mathbf{k}_\parallel, k_z)]$ over k_z. This is carried out using an in-house *ab initio* tight-binding (TB) code [21]. Details of band structure and magnetocrystalline calculations can be found elsewhere [22].

III. RESULTS AND DISCUSSION

A. X-ray

The crystal structure and lattice constants were obtained by the refinement of powder x-ray diffraction measurements of crushed single crystals of TbV_6Sn_6. Refinement solutions were determined using the MAUD software package [20]. Impurity phases including Sn residue were determined to be less than 1% of the total material measured. Cell refinement in the hexagonal space group $P6/mmm$ determined the lattice constants to be $a = 5.519 \pm 0.001$ Å and $c = 9.181 \pm 0.002$ Å. The crystal structure of TbV_6Sn_6 is shown in Fig. 1(a). The microstructure parameters derived from the refinement are listed in Table I. The refinement is shown in Fig. 1(c) ($R = 0.203$) alongside the residuals. The derived crystal structure is consistent with previous measurements of the rare-earth substituted GdV_6Sn_6 and YV_6Sn_6 [12].

B. Heat capacity

The heat capacity measurements are summarized in Fig. 1(b). There is a sharp mean-field-like step observed at 4.1 K. This step is broadened considerably by the application of relatively small magnetic fields, until the transition is no longer observable above around 0.5 T. This, along with magnetic measurements shown in Fig. 2, is suggestive that the conjugate field to the phase transition is a magnetic field along the *c*-axis. The entropy (integrated from C_p/T, which was interpolated assuming it is a smooth monotonic function of temperature with value 0 at 0 K) approaches a value near R ln(2) at the phase transition. Note that this integration was done after removing the heat capacity from YV_6Sn_6, a nonmagnetic analog of TbV_6Sn_6. This suggests the phase transition is Ising-like in that it involves the splitting of a degenerate magnetic doublet. The shape of the heat capacity below the phase transition also strongly resembles the heat capacity signature of a canonical spin-1/2 Ising phase transition.

C. Magnetic susceptibility and magnetization versus field

Magnetic susceptibility measurements performed at 500 Oe are depicted in Fig. 2(a), with the red curves indicating the magnetic field is along the *c*-axis and the blue curves (multiplied by 25) with the field along the *ab*-plane. Zero-field-cooled (ZFC) and field-cooled (FC) measurements were

TABLE I. Microstructure parameters determined for the TbV_6Sn_6 unit cell in the $P6/mmm$ hexagonal space group symmetry. The lattice constants were determined to be $a = 5.519 \pm 0.001$ Å and $c = 9.181 \pm 0.002$ Å. The occupancy listed provided the best fit of the measured x-ray diffraction data but only marginally improved the fit quality.

Atom (site)	*x*	*y*	*z*	Occupancy
Tb	1	1	0.5	1
V	0.5	0.5	0.7515	1
Sn1	1	1	0.8317	0.97
Sn2	0.3333	0.6667	0.5	0.90
Sn3	0.3333	0.6667	1	0.92

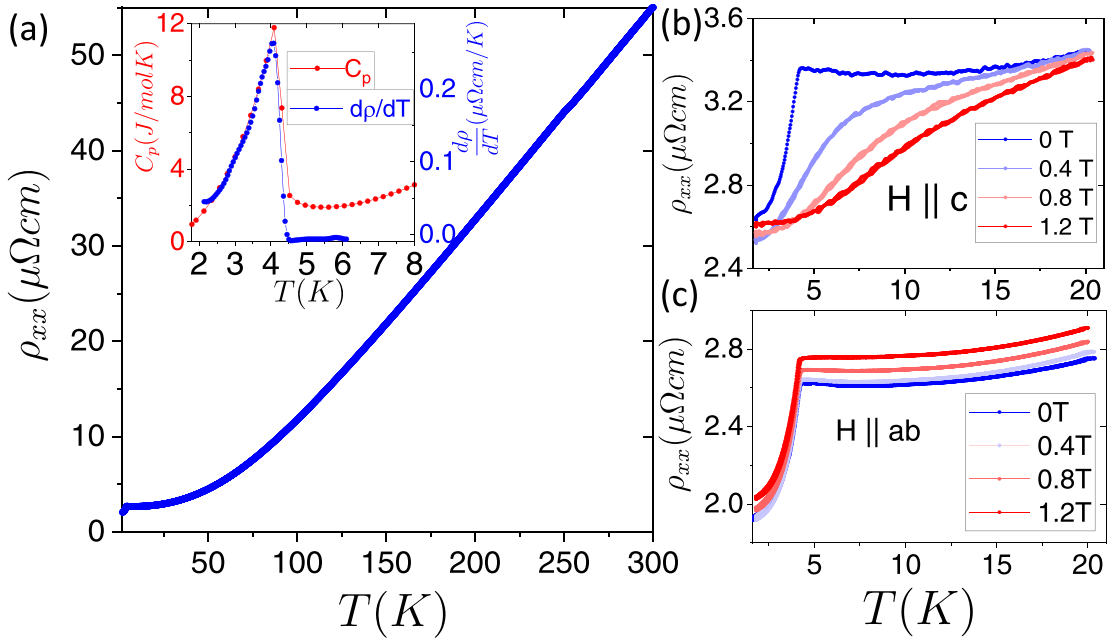

FIG. 3. (a) In-plane resistivity vs temperature from 2 to 300 K. (b) Resistivity vs temperature data with magnetic fields applied along the *c*-axis, and similarly to the heat capacity the signature of the phase transition is broadened considerably above 0.5 T. (c) Resistivity vs temperature curves with magnetic field applied along the *ab*-plane, and the application of this field does not shift or broaden the phase transition noticeably.

performed, and hysteretic behavior indicative of domains is present for both orientations. However there is a striking magnetic anisotropy evident in this material, as the magnetic susceptibility along the *c*-axis is nearly 75 times the magnetic susceptibility along the *ab*-plane at temperatures just above the phase transition. Even up to 200 K, the *c*-axis susceptibility remains more than twice as large as the in-plane susceptibility. Magnetization versus field (MvH) measurements are also displayed in Fig. 2(b) with H oriented along the *c*-axis from 2 to 7 K, and there are clear signs of hysteresis for temperatures below 4 K, but not above. These data are offset by $10\mu_B$/f.u. for clarity. In-plane MvH measurements performed up to 14 T [shown up to 2 T in the inset to Fig. 2(a)] can be extrapolated to determine the magnetic anisotropy energy of this compound at nearly 330 K/f.u., larger than that of canonical uniaxial ferromagnets like $LiHoF_4$ [23]. This value was determined by finding the area enclosed between the out-of-plane and in-plane magnetization curves [24], namely

$$K_{\text{eff}} = \int_0^{\mu_0 H_S} (M_{\text{OOP}} - M_{\text{IP}})\, d(\mu_0 H), \qquad (1)$$

where K_{eff} is the effective magnetic anisotropy energy, H_S is the extrapolated in-plane saturation field, and M_{OOP} and M_{IP} are the out-of-plane and in-plane magnetizations, respectively.

The magnetic anisotropy energy was also calculated from first principles, and the results as a function of angle θ from the *c*-axis are shown in Fig. 2(c). The difference in the anisotropy energy between 0° and 90° was calculated to be roughly 17.5 meV/f.u. (203 K/f.u.), which is consistent with the large value found from MvH measurements.

D. Resistivity and magnetotransport

The in-plane resistivity versus temperature is shown in Fig. 3(a). There is a clear and pronounced kink at 4.1 K, shown more clearly in Fig. 3(b) at 0 T. In the inset of Fig. 3(a), the heat capacity and $d\rho/dT$ are shown, and they display a similar temperature dependence in the proximity of the ferromagnetic phase transition, indicating that the classic Fisher-Langer argument [25] is relevant for this compound. This implies that the magnetic fluctuations that result from the phase transition play a similarly dominant role in determining both the energy of the system and the scattering rate of the longitudinal resistivity at low temperatures. Figure 3(b) displays resistivity versus temperature data with magnetic fields applied along the *c*-axis, and similarly to the heat capacity the signature of the phase transition is broadened considerably above 0.5 T. Figure 3(c) displays resistivity versus temperature curves with magnetic field applied along the *ab*-plane, and the application of fields up to 1.2 T does not shift or broaden the phase transition noticeably.

E. Hall measurements

Hall measurements were performed from 300 to 1.7 K with fields being swept in both directions. We first focus on low-field data near the transition temperature where an AHE emerges. As shown in Fig. 4(a), there is hysteresis in ρ_{xy} below 4 K at field scales similar to those observed to be relevant to the hysteresis of the magnetization. Subtracting the linear background above the saturation field reveals the close resemblance between $\Delta\rho_{xy}$ [Figs. 4(b) and 4(c)] and magnetization (Fig. 2), unambiguously establishing the existence of an AHE. Note that the data in Fig. 4(c) have been offset by 0.05 $\mu\Omega$ cm for clarity. We next turn to the high-field

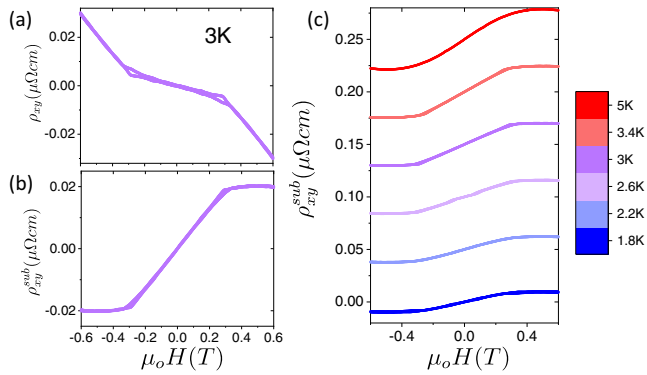

FIG. 4. (a) Antisymmetrized ρ_{xy} data vs field at low fields at 3 K. There is a noticeable hysteresis in the data, indicative of an anomalous Hall contribution. (b) Same as (a) but subtracted by a high-field linear fit. (c) Similar data (offset by 0.05 $\mu\Omega$ cm for clarity) with subtracted linear backgrounds at temperatures from 1.8 to 5 K, suggestive that an anomalous Hall contribution exists at temperatures below and above the ferromagnetic phase transition.

data, shown in Fig. 5, where ρ_{xy} is dominated by the ordinary Hall effect. As the magnetic field increases well beyond the saturation field (0.5 T), the ordinary Hall resistivity exhibits a nonlinear magnetic field dependence at temperatures up to around 150 K, indicating two-band behavior. Following the procedure described in [26], two-band fitting was performed to extract the hole and electron mobilities and carrier densities, shown in the right panels of Fig. 5. Although the fitting is not quantitatively precise (described in detail in the supplemental material [27]), especially at temperatures in which the Hall resistivity can be described effectively by a one-band model, we can still draw robust conclusions that the hole and electron mobilities increase significantly as temperature is decreased, and that the electron carrier density is larger than the hole carrier density at all temperatures, which leads to a positive Hall coefficient at temperatures where effective one-band Hall transport is observed.

F. ARPES measurements

To investigate the electronic structure, we measured the normal-state electronic structure of TbV_6Sn_6 at 15 K using ARPES (Fig. 6). We found two types of terminations, distinguished by the different valence-band structures as well as core-level spectroscopy. Consistent with previous work on Ho/GdV_6Sn_6 [15], the two terminations correspond to the kagome termination and the Sn termination. In Fig. 6 we present the results from the kagome termination. Typical of vanadium kagome systems, the Fermi surface exhibits triangular pockets centered at the K points of the Brillouin zone (BZ) with tips of the triangles meeting at the M points. Band dispersions along high-symmetry directions are also shown, taken with different polarizations [Figs. 6(b) and 6(c)]. For comparison, we also show the density functional theory (DFT) calculated bulk bands integrated along k_z. There is overall good agreement between calculated and measured dispersions. In particular, we identify the presence of a Dirac crossing near -0.2 eV at the K point that disperses up to a saddle point near the Fermi level at the M point, which is also captured in the DFT calculations. The overall electronic structure of the normal state of TbV_6Sn_6 resembles that of Ho/GdV_6Sn_6 [15]. We also note that the kagome flat bands according to DFT appear near -1 eV. We do not observe

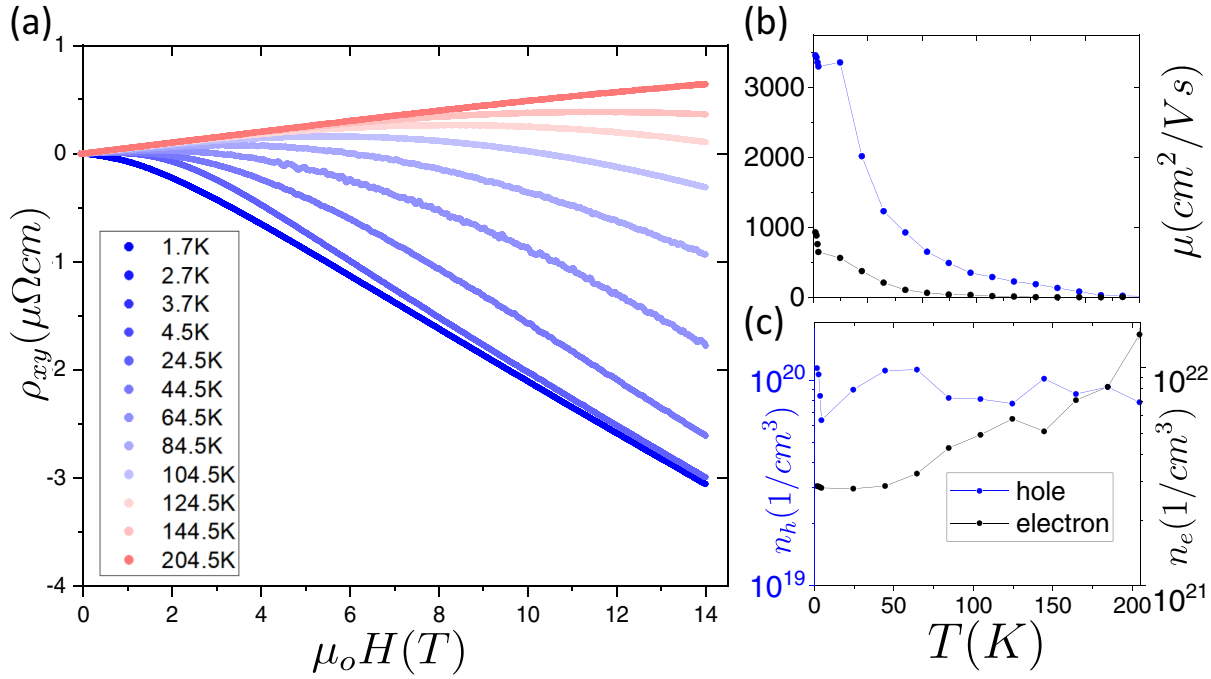

FIG. 5. (a) Hall measurements from 200 to 1.7 K with fields sweeping from 0 to 14 T, then down to -14 T and back to 0 T. Only the antisymmetrized data at positive fields is shown. (b) Mobilities and (c) carrier densities extracted from two-band fitting of Hall measurements. Both the electron and hole mobilities increase substantially as the temperature is decreased, consistent with previous measurements of YV_6Sn_6.

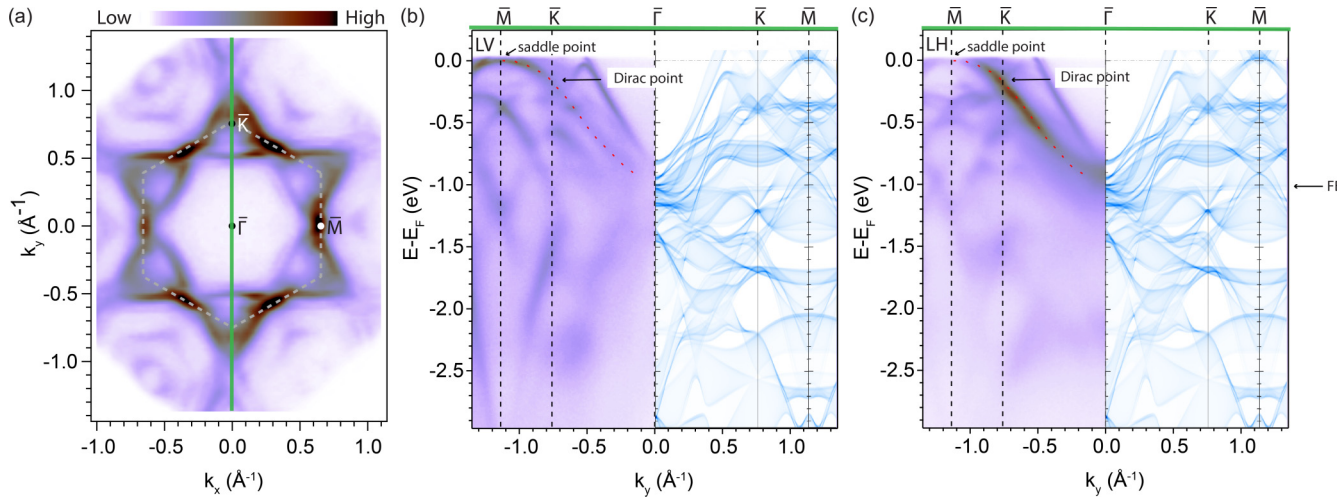

FIG. 6. Electronic structure of the kagome termination of TbV_6Sn_6. (a) Fermi surface of TbV_6Sn_6 measured with linear horizontal (LH) polarization. The white dashed line denotes the first Brillouin zone. (b) $\bar{\Gamma} - \bar{K} - \bar{M}$ cut measured with linear vertical (LV) polarization. DFT calculated dispersions along the same cut integrated along k_z are shown for comparison. (c) Same as (b) but measured with LH polarization. Dirac point and saddle point are marked. All measurements were performed with 83 eV photons at 15 K.

strong intensity of the flat bands in this energy range, possibly due to the strong k_z dispersion of the kagome flat bands resulting from finite interlayer interactions, which, coupled with the k_z broadening effect due to the poor out-of-plane resolution of the photoemission process, makes the dispersive flat bands harder to resolve.

IV. DISCUSSION

YV_6Sn_6, which is nearly identical to TbV_6Sn_6 except that the rare-earth site has been replaced with an ion with no $4f$ electrons, has been measured recently and found to have no magnetic order or evident magnetic anisotropy down to 1.7 K [12]. Thus the cause of the ferromagnetic phase transition in TbV_6Sn_6 is from the cooperative alignment of the $4f$ electrons of the Tb^{3+} ion. The magnetic anisotropy seen in this material can be understood as a consequence of the relevant energy scales for the $4f$ sublattice.

The finer details of $4f$ energy scales have been explained elsewhere [28,29], but here is a brief summary. The hierarchy of energy scales starts with Coulomb repulsion (which manifests in Hunds' rules, which determine the filling of the $4f$ orbitals.) Spin-orbit coupling determines the total angular momentum number $J = L + S$ to be the good quantum number for the $4f$ electronic multiplet, and then the perturbative crystalline electric field (CEF) potential from the surrounding environment splits the $2J + 1$ degenerate states. The multiplicity of the degeneracies of the CEF spectrum is determined by the point-group symmetry surrounding the $4f$ ion. In the case of the Tb ion in a D_{6h} point-group symmetry, the eight $4f$ electrons form a $J = 6$ electronic multiplet, and the 13 degenerate states are split into five singlets and four doublets. However, only the degeneracies can be known *apriori* (from the dimensions of the corresponding irreducible representations), but the eigenenergies cannot be determined without knowing microscopic details of the surrounding ligands.

Group theory considerations (see the supplemental material [27]) also fix the constituent m_j states of the different CEF states. In the case of the two different types (irreducible representations) of doublets allowed in D_{6h} for $J = 6$, the E_{1g} doublet is composed of $m_j = \pm 4$ and ± 2 states, and the E_{2g} doublet is composed of ± 5 and ± 1 states. A CEF spectrum, which would explain both the heat capacity and the extreme magnetic anisotropy, would be one in which the ground state is one of the aforementioned doublets, and that the next-nearest excited state was $\Delta_{CEF} > 100$ K above. Common energy scales for CEF splittings can be 100 K or higher. Because $\langle E^n_{ig}|J_x|E^m_{ig}\rangle = 0$ for both doublets E_{1g} and E_{2g} (n and m here represent each doublet state), there would be no magnetic susceptibility in the ab-plane from the $4f$ ground state, and the susceptibility would only become more isotropic at temperatures at and above Δ_{CEF}. This ground state could of course be polarized in the z-direction, and $4f$ sublattice sites could cooperatively align ferromagnetically along the c-axis, providing an entropy of $R\ln(2)$ at the phase transition. A more thorough calculation was performed to assess the magnetic energy of the $4f$ electrons of Tb as a function of angle from the z-axis [depicted in Fig. 2(c)], explicitly considering the Hamiltonian arising from considering both spin-orbit coupling and crystal-field terms that can be approximated from the atomic spacings.

The single-ion magnetic anisotropy of the Tb ion presumably plays the dominant role in determining the magnetic easy-axis of TbV_6Sn_6 at all temperatures. This is in contrast with the more complicated case of $TbMn_6Sn_6$, in which the magnetic anisotropy energy scales of the Tb ions and the Mn layers compete, leading to an in-plane to out-of-plane rotation of magnetic order at $T_{sr} = 309$ K, and lower temperature metamagnetic transitions with an in-plane applied field [18,30]. It has been calculated [30] that the magnetic Tb ions in this material have a similarly large single-ion magnetic anisotropy as was calculated for TbV_6Sn_6 in Fig. 2(c), and so our experimental results are consistent with the V kagome layers not affecting the magnetic anisotropy of the system, also explaining the overall smaller magnetic exchange interaction between only Tb ions, which results in $T_c = 4.1$ K.

An intriguing question is whether the Ising ferromagnetism in TbV_6Sn_6 may lead to the formation of exotic phases, such as Chern gapped Dirac fermions in the bulk, or a quantum anomalous Hall surface state. Previous density functional theory calculations suggested that the electronic structures of several RV_6Sn_6 compounds can be characterized as that of a topological metal, with surface states originating from the nontrivial $\mathbb{Z}_2$ indices associated with the occupied bands [12]. Our ARPES measurements are consistent with others that have revealed bulk bands with Dirac dispersion near the K point of the Brillouin zone [15]. The observed anomalous Hall effect of TbV_6Sn_6 is a clear signature of the impact of magnetism on the itinerant electrons. Using the anomalous Hall resistivity and longitudinal resistivity, we calculated the value of anomalous Hall conductivity at 1.8 K to be approximately 2000 $\Omega^{-1}\,\mathrm{cm}^{-1}$. This value, together with the value of the conductivity, puts the anomalous Hall effect of TbV_6Sn_6 at the boundary between being dominated by skew-scattering or arising from an intrinsic effect [31]. In principle, the intrinsic contribution of AHE can be extracted by a scaling analysis via the equation

$$\rho_{\mathrm{AH}} = a\rho_{xx} + b\rho_{xx}^2, \tag{2}$$

where the first term arises from skew scattering and the second term is due to Berry curvature and side-jump mechanisms. This would be possible if the AHE could be extracted in a parameter range where the resistivity varies by orders of magnitude [31]. However, due to the low Curie temperature, the longitudinal resistivity changes very little in the temperature range where we observed the AHE. Future studies of AHE as a function of mean free path by systematically introducing disorder are needed to address this issue.

V. CONCLUSIONS

The synthesis of the vanadium-based kagome metal TbV_6Sn_6 single crystals is presented, and it was determined via powder x-ray diffraction to be of the same crystal structure type ($MgFe_6Ge_6$) and have the same space-group symmetry ($P6/mmm$) as the recently discovered YV_6Sn_6 and GdV_6Sn_6. It was shown to have a ferromagnetic phase transition at 4.1 K likely involving the cooperative alignment of the $4f$ electrons of the Tb^{3+} ion. This compound displays a striking magnetic anisotropy, with magnetic susceptibility and MvH measurements confirming that the c-axis is the magnetic easy axis and an extrapolated magnetic anisotropy energy of above 330 K at 2.5 K, making this material one of the "most uniaxial" ferromagnets known at low temperatures. The heat capacity signature and entropy (extrapolated) at the phase transition provide evidence that it is an effective spin-1/2 Ising phase transition, possibly involving the spontaneous splitting of a $4f$ ground-state doublet. This study demonstrates the tunability of the magnetism in RV_6Sn_6 in the presence of a kagome lattice.

ACKNOWLEDGMENTS

This work is supported by the Air Force Office of Scientific Research under Grant No. FA9550-21-1-0068, the David and Lucile Packard Foundation, and the Gordon and Betty Moore Foundation's EPiQS Initiative, Grant No. GBMF6759 to J.-H.C. The work at Berkeley and LBNL was funded by the U.S. Department of Energy, Office of Science, Office of Basic Energy Sciences, Materials Sciences and Engineering Division under Contract No. DE-AC02-05-CH11231 (Quantum Materials program KC2202). The work at Rice was funded by the Robert A. Welch Foundation Grant No. C-2024 and the Gordon and Betty Moore Foundation's EPiQS Initiative through Grant No. GBMF9470. Use of the Stanford Synchrotron Radiation Lightsource, SLAC National Accelerator Laboratory, is supported by the U.S. Department of Energy, Office of Science, Office of Basic Energy Sciences under Contract No. DE-AC02-76SF00515. L.K. and Y.L. are supported by the U.S. Department of Energy, Office of Science, Office of Basic Energy Sciences, Materials Sciences and Engineering Division, and Early Career Research Program.

[1] L. Ye, M. Kang, J. Liu, F. von Cube, C. R. Wicker, T. Suzuki, C. Jozwiak, A. Bostwick, E. Rotenberg, D. C. Bell, L. Fu, R. Comin, and J. G. Checkelsky, Massive dirac fermions in a ferromagnetic kagome metal, Nature (London) **555**, 638 (2018).

[2] M. Kang, L. Ye, S. Fang, J.-S. You, A. Levitan, M. Han, J. I. Facio, C. Jozwiak, A. Bostwick, E. Rotenberg, M. K. Chan, R. D. McDonald, D. Graf, K. Kaznatcheev, E. Vescovo, D. C. Bell, E. Kaxiras, J. van den Brink, M. Richter, M. Prasad Ghimire, J. G. Checkelsky, and R. Comin, Dirac fermions and flat bands in the ideal kagome metal FeSn, Nat. Mater. **19**, 163 (2020).

[3] M. Kang, S. Fang, L. Ye, H. C. Po, J. Denlinger, C. Jozwiak, A. Bostwick, E. Rotenberg, E. Kaxiras, J. G. Checkelsky, and R. Comin, Topological flat bands in frustrated kagome lattice CoSn, Nat. Commun. **11**, 4004 (2020).

[4] J.-X. Yin, S. S. Zhang, H. Li, K. Jiang, G. Chang, B. Zhang, B. Lian, C. Xiang, I. Belopolski, H. Zheng, T. A. Cochran, S.-Y. Xu, G. Bian, K. Liu, T.-R. Chang, H. Lin, Z.-Y. Lu, Z. Wang, S. Jia, W. Wang, and M. Z. Hasan, Giant and anisotropic many-body spin–orbit tunability in a strongly correlated kagome magnet, Nature (London) **562**, 91 (2018).

[5] J.-X. Yin, S. S. Zhang, G. Chang, Q. Wang, S. S. Tsirkin, Z. Guguchia, B. Lian, H. Zhou, K. Jiang, I. Belopolski, N. Shumiya, D. Multer, M. Litskevich, T. A. Cochran, H. Lin, Z. Wang, T. Neupert, S. Jia, H. Lei, and M. Z. Hasan, Negative flat band magnetism in a spin–orbit-coupled correlated kagome magnet, Nat. Phys. **15**, 443 (2019).

[6] N. J. Ghimire, R. L. Dally, L. Poudel, D. C. Jones, D. Michel, N. T. Magar, M. Bleuel, M. A. McGuire, J. S. Jiang, J. F. Mitchell, J. W. Lynn, and I. I. Mazin, Competing magnetic phases and fluctuation-driven scalar spin chirality in the kagome metal YMn_6Sn_6, Sci. Adv. **6**, eabe2680 (2020).

[7] B. R. Ortiz, L. C. Gomes, J. R. Morey, M. Winiarski, M. Bordelon, J. S. Mangum, I. W. H. Oswald, J. A. Rodriguez-Rivera, J. R. Neilson, S. D. Wilson, E. Ertekin, T. M. McQueen, and E. S. Toberer, New kagome prototype materials: Discovery

of KV_3Sb_5, RbV_3Sb_5, and CsV_3Sb_5, Phys. Rev. Mater. **3**, 094407 (2019).

[8] B. R. Ortiz, S. M. L. Teicher, Y. Hu, J. L. Zuo, P. M. Sarte, E. C. Schueller, A. M. Milinda Abeykoon, M. J. Krogstad, S. Rosenkranz, R. Osborn, R. Seshadri, L. Balents, J. He, and S. D. Wilson, CsV_3Sb_5: A Z_2 Topological Kagome Metal with a Superconducting Ground State, Phys. Rev. Lett. **125**, 247002 (2020).

[9] J.-X. Yin, W. Ma, T. A. Cochran, X. Xu, S. S. Zhang, H.-J. Tien, N. Shumiya, G. Cheng, K. Jiang, B. Lian, Z. Song, G. Chang, I. Belopolski, D. Multer, M. Litskevich, Z.-J. Cheng, X. P. Yang, B. Swidler, H. Zhou, H. Lin, T. Neupert, Z. Wang, N. Yao, T.-R. Chang, S. Jia, and M. Zahid Hasan, Quantum-limit Chern topological magnetism in $TbMn_6Sn_6$, Nature (London) **583**, 533 (2020).

[10] W. Ma, X. Xu, J.-X. Yin, H. Yang, H. Zhou, Z.-J. Cheng, Y. Huang, Z. Qu, F. Wang, M. Z. Hasan, and S. Jia, Rare Earth Engineering in RMn_6Sn_6 (R = Gd - Tm, Lu) Topological Kagome Magnets, Phys. Rev. Lett. **126**, 246602 (2021).

[11] D. Chen, C. Le, C. Fu, H. Lin, W. Schnelle, Y. Sun, and C. Felser, Large anomalous Hall effect in the kagome ferromagnet $LiMn_6Sn_6$, Phys. Rev. B **103**, 144410 (2021).

[12] G. Pokharel, S. M. L. Teicher, B. R. Ortiz, P. M. Sarte, G. Wu, S. Peng, J. He, R. Seshadri, and S. D. Wilson, Study of the electronic properties of topological kagome metals YV_6Sn_6 and GdV_6Sn_6, Phys. Rev. B **104**, 235139 (2021).

[13] H. Ishikawa, T. Yajima, M. Kawamura, H. Mitamura, and K. Kindo, Gdv_6sn_6: A multi-carrier metal with non-magnetic 3d-electron kagome bands and 4f-electron magnetism, J. Phys. Soc. Jpn. **90**, 124704 (2021).

[14] H. W. Suriya Arachchige, W. R. Meier, M. Marshall, T. Matsuoka, R. Xue, M. A. McGuire, R. P. Hermann, H. Cao, and D. Mandrus, Charge density wave in kagome lattice intermetallic ScV_6Sn_6, arXiv:2205.04582.

[15] S. Peng, Y. Han, G. Pokharel, J. Shen, Z. Li, M. Hashimoto, D. Lu, B. R. Ortiz, Y. Luo, H. Li, M. Guo, B. Wang, S. Cui, Z. Sun, Z. Qiao, S. D. Wilson, and J. He, Realizing Kagome Band Structure in Two-Dimensional Kagome Surface States of RV_6Sn_6 (R = Gd, Ho), Phys. Rev. Lett. **127**, 266401 (2021).

[16] Y. Hu, X. Wu, Y. Yang, N. Plumb, A. Schnyder, W. Xie, J. Ma, and M. Shi, arXiv:2205.15927.

[17] L. Gao, S. Shen, Q. Wang, W. Shi, Y. Zhao, C. Li, W. Cao, C. Pei, J.-Y. Ge, G. Li, J. Li, Y. Chen, S. Yan, and Y. Qi, Anomalous Hall effect in ferrimagnetic metal RMn_6Sn_6 (R = Tb, Dy, Ho) with clean Mn kagome lattice, Appl. Phys. Lett. **119**, 092405 (2021).

[18] D. M. Clatterbuck and K. A. Gschneidner Jr, Magnetic properties of RMn_6Sn_6 (R = Tb, Ho, Er, Tm, Lu) single crystals, J. Magn. Magn. Mater. **207**, 78 (1999).

[19] P. C. Canfield, T. Kong, U. S. Kaluarachchi, and N. H. Jo, Use of frit-disc crucibles for routine and exploratory solution growth of single crystalline samples, Philos. Mag. **96**, 84 (2016).

[20] L. Lutterotti, M. Bortolotti, G. Ischia, and I. Lonardelli, Rietveld texture analysis from diffraction images, Eur. Powder Diffr. Conf. **26**, 125 (2007).

[21] L. Ke, Intersublattice magnetocrystalline anisotropy using a realistic tight-binding method based on maximally localized Wannier functions, Phys. Rev. B **99**, 054418 (2019).

[22] Y. Lee, R. Skomski, X. Wang, P. P. Orth, A. K. Pathak, B. N. Harmon, R. J. McQueeney, I. I. Mazin, and L. Ke, Interplay between magnetism and band topology in Kagome magnets RMn_6Sn_6, arXiv:2201.11265.

[23] P. Beauvillain, J. P. Renard, I. Laursen, and P. J. Walker, Critical behavior of the magnetic susceptibility of the uniaxial ferromagnet $LiHoF_4$, Phys. Rev. B **18**, 3360 (1978).

[24] M. T. Johnson, P. J. H. Bloemen, F. J. A. den Broeder, and J. J. de Vries, Magnetic anisotropy in metallic multilayers, Rep. Prog. Phys. **59**, 1409 (1996).

[25] M. E. Fisher and J. S. Langer, Resistive Anomalies at Magnetic Critical Points, Phys. Rev. Lett. **20**, 665 (1968).

[26] S. M. Watts, S. Wirth, S. von Molnar, A. Barry, and J. M. D. Coey, Evidence for two-band magnetotransport in half-metallic chromium dioxide, Phys. Rev. B **61**, 9621 (2000).

[27] See the Supplemental Material at http://link.aps.org/supplemental/10.1103/PhysRevB.106.115139 for additional information on the two-band Hall fitting and the group theory relevant to the CEF argument.

[28] P. Morin and D. Schmitt, Quadrupole interactions in rare-earth intermetallic compounds, J. Phys. (Paris) Colloq. **49**, C8-321 (1988).

[29] A. V. Maharaj, E. W. Rosenberg, A. T. Hristov, E. Berg, R. M. Fernandes, I. R. Fisher, and S. A. Kivelson, Transverse fields to tune an Ising-nematic quantum phase transition, Proc. Natl. Acad. Sci. (USA) **114**, 13430 (2017).

[30] D. C. Jones, S. Das, H. Bhandari, X. Liu, P. Siegfried, M. P. Ghimire, S. S. Tsirkin, I. I. Mazin, and N. J. Ghimire, Origin of spin reorientation and intrinsic anomalous Hall effect in the kagome ferrimagnet $TbMn_6Sn_6$, arXiv:2203.17246.

[31] Y. Tian, L. Ye, and X. Jin, Proper Scaling of the Anomalous Hall Effect, Phys. Rev. Lett. **103**, 087206 (2009).